analytical chemistry

pubs.acs.org/ac Article

A Multiplexed Self-Powered Dual-Photoelectrode Biosensor for Detecting Dual Analytes Based on an Electron-Transfer-Regulated Conversion Strategy

Jie Wei, Qinqin Hu, Yun Gao, Nan Hao, Jing Qian, and Kun Wang*

Cite This: *Anal. Chem.* 2021, 93, 6214−6222 Read Online

ACCESS | Metrics & More | Article Recommendations | Supporting Information

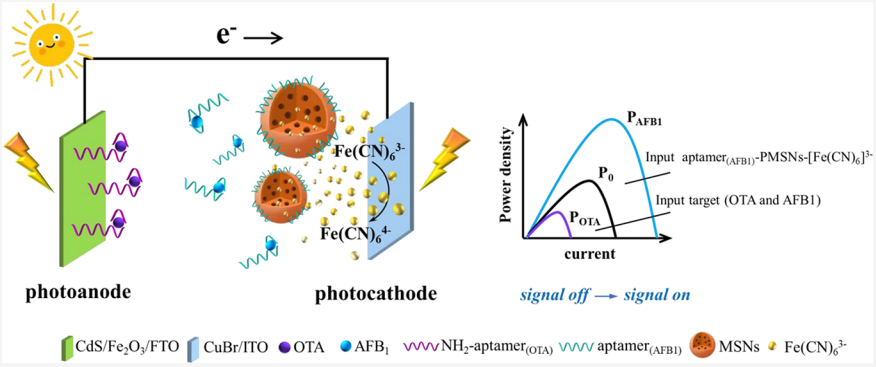

ABSTRACT: Due to the inherent mechanism limitation of photocatalytic fuel cell based self-powered biosensors (PFC-SPBs), it was difficult to distinguish the power density of various photoactive materials or recognition events in one detection process, which made it lack multitarget quantitative capacity. In order to solve this problem, we proposed an electron-transfer-regulated conversion strategy for the construction of multiplexed PFC-SPBs. Herein, the n-type CdS/Fe_2O_3 nanorod array (NR) heterojunction and p-type CuBr semiconductor were used as photoactive materials to prepare the photoanode and photocathode. Based on the appropriate Fermi level differentiation between these two photoelectrodes, a self-powered sensing platform driven by visible light without external energy supply was achieved. In this design, two kinds of common and easily coexisting mycotoxins OTA and AFB1 acted as model analytes. The coupling of "signal off" and "signal on" was realized by controlling the electronic transmission on the interface between the photoanode and photocathode, so as to achieve the simultaneous detection of two mycotoxins. This work established a proof-of-concept for the integration of a dual-photoelectrode with dual-assay that could provide the innovative inspiration for the formation of a general multiplexed self-powered sensing platform.

1. INTRODUCTION

Photocatalytic fuel cell based self-powered biosensors (PFC-SPBs), as the next generation of sensing platforms, not only inherit the merits of electrochemical technology,[1,2] such as high sensitivity,[3] rapid response,[4] and simple equipment,[5] but also have better performance in selectivity, miniaturization, high efficiency, and low cost.[6] PFC-SPBs rely on a two-electrode system (only a cathode and an anode without a reference electrode), which simplifies the structure and facilitates the integration of the device.[7] Moreover, it could convert light and chemical energy into electricity simultaneously, creating more energy utilization.[8] Due to the absence of external voltage, the nonspecific redox reaction of electroactive interferences could be effectively prevented, avoiding the false positive results. Depending on these fascinating characteristics, various PFC-SPBs have been constructed,[9−11] and most of them used photosensitive semiconductors as a photoanode or a photocathode in the formation of single-photoelectrode PFC-SPBs. Another electrode was selected with precious metal Pt,[12] Prussian blue,[13] or electroactive materials.[14] In our previous work,[15] we designed a dual-photoelectrode PFC-SPB with TiO_2 nanoparticles as a photoanode and nitrogen-doped graphene-BiOBr as a photocathode. By increasing the absorption and conversion of light, the energy utilization was improved and the use of an expensive Pt electrode was avoided.

Although the aforementioned works have made great contributions to the development of PFC-SPBs, they still lacked multitarget quantitative capacity.[16−18] The design

Received: February 3, 2021
Accepted: March 30, 2021
Published: April 8, 2021

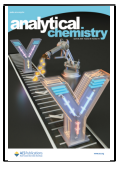

https://doi.org/10.1021/acs.analchem.1c00503
Anal. Chem. 2021, 93, 6214−6222

strategy of multiplexed PFC-SPBs was different from numerous studies of electrochemistry,[19,20] photoelectrochemistry,[21] fluorescence,[22] and electrochemiluminescence biosensors.[23] Owing to the inherent mechanism of the photocatalytic fuel cell (PFC) technique, it was difficult to distinguish the power density from various photoactive materials or recognition events in one detection process. Meanwhile, the common multitarget analysis methods, such as the wavelength-resolved strategy,[24] potentiometric-resolved strategy,[25] and light addressing strategy,[26] were not suitable for the construction of PFC-SPBs. For instance, the photoactive materials used in the wavelength-resolved strategy must be wavelength selective and had a narrow spectral response range to ensure that the excitation wavelengths of each material could not overlap and energy transfer could not occur.[27] As a result, it was difficult to select suitable photoactive materials and high requirements for the illuminant. An instrument with continuously adjustable wavelength and monochromaticity was needed, which increased the cost.[28] For the potentiometric-resolved strategy, an appropriate bias voltage must be applied to make one of the photoactive materials not produce photocurrent at the critical voltage, so as to identify the signal response of another photoactive material.[29,30] However, there is no need to exert external voltage to generate a signal in the self-powered detection, which limited the application of this strategy. In addition, although the light addressing strategy could realize the simultaneous detection of multitargets, it required a small enough excitation beam and the uniform excitation of each area, and it also put forward a higher demand for the precision of electrode array modification.[31]

To date, the research on PFC-SPBs is only in the initial phase; almost no efforts have been devoted to the construction of multiplexed PFC-SPBs. However, it is particularly valuable in the practical application, especially for agricultural products which are easily contaminated by many types of mycotoxins. According to the research, due to the various fungi requiring similar environments in their growth or toxigenic conditions, 91.4% of contaminated samples have detected two or more kinds of mycotoxins at the same time.[32] Notably, the co-occurrence of mycotoxins in the same agricultural product could display obvious synergistic or additive damage for human or animal health.[33,34] For example, ochratoxin A (OTA) and aflatoxin B1 (AFB1) usually coexist in moldy maize and its products, engendering a combined toxicity than the total harm caused by each toxin.[35] Therefore, it is urgent to establish a simple, sensitive, and low-cost multiplexed technology for simultaneous monitoring of OTA and AFB1 in farm goods. Compared with the method that only responds to a single target, the multiplexed assay exhibited more advantages including the increased analysis throughput, reduced time and procedures, less sample usage, and lower cost. Thus, such a multiplexed PFC-SPB could bring great convenience and provide more comprehensive results for mycotoxin screening.

Herein, a multiplexed dual-photoelectrode PFC-SPB based on an electron-transfer-regulated conversion strategy was fabricated. CdS sensitized Fe_2O_3 nanorod array (NR) heterojunctions and CuBr semiconductors have been used in the preparation of photoanodes and photocathodes due to their excellent physicochemical properties and photoelectric conversion performance. According to the appropriate differentiation of Fermi level between the photoanode and photocathode, the self-bias voltage was generated to drive the transfer of photoinduced electrons, realizing the PFC-SPB that could provide energy during the detection. These dual-photoelectrodes with excellent photoelectric conversion capacity improved the utilization of light energy and ensured the stable and efficient signal output. Due to the steric hindrance effect of the photoanode produced by the combination of $aptamer_{(OTA)}$ and target, the electron transmission between interfaces was inhibited, thus forming a "signal-off" OTA detection. Then, the positively charged mesoporous silicon dioxide nanospheres (PMSNs) with high specific surface area were used as carriers to fix $aptamer_{(AFB1)}$ and the electron capture agent ($[Fe(CN)_6]^{3-}$) for AFB_1 detection. The $[Fe(CN)_6]^{3-}$ was released in the pore of PMSNs via the specific recognition between $aptamer_{(AFB1)}$ and AFB1. As an electron acceptor, it accelerated the electron transfer and consumption in the external circuit, thus presenting a "signal-on" response for AFB1 detection. Based on the electron-transfer-regulated "on−off−on" conversion of power density, this multiplexed PFC-SPB could obtain the specific and sensitive dual-assay of OTA and AFB1, which has not been reported to our knowledge.

2. EXPERIMENTAL SECTION

2.1. Fabrication of the CdS/Fe_2O_3 NRs/FTO Photoanode. The Fe_2O_3 nanorod arrays (NRs) were in situ grown on FTO substrate using a modified hydrothermal method and calcination treatment.[36] First, 1.01 g of $FeCl_3·6H_2O$ and 0.33 g of urea were dissolved in 30 mL of deionized water. The mixture was stirred for 20 min to make it completely dissolved and then poured into the Teflon-lined stainless steel autoclave. Then, two pieces of fluorine-doped tin oxide (FTO) glass were immersed into the reactor with the conductive side downward. After hydrothermal reaction at 100 °C for 12 h, the FeOOH NRs/FTO were washed with ultrapure water to remove the impurities adsorbed on the surface and then annealed at 700 °C for 15 min to form the Fe_2O_3 NRs/FTO.

CdS/Fe_2O_3 NRs/FTO were fabricated by chemical bath deposition. Briefly, 1.19 g of $CdCl_2$, 2.03 g of NH_4Cl, and 1.37 g of thiourea were mixed in 500 mL of ammonia solution (0.76 mol/L). Then, the prepared Fe_2O_3 NRs/FTO were put into this mixture and reacted at 80 °C for 20 min for CdS deposition. After that, the products were washed and annealed at 400 °C for 1 h to obtain the CdS/Fe_2O_3 NRs/FTO as the photoanode.

2.2. Fabrication of the CuBr/ITO Photocathode. CuBr was used as photoactive material to prepare the photocathode. The Kapton tape was sealed on the cleaned indium tin oxide (ITO) glass to determine the working area of 0.5 × 0.5 cm^2. After that, 20 mg of CuBr was dispersed in 1 mL of *N*,*N*-dimethylformamide, and then, 20 μL of the above dispersion was added onto the ITO substrate. After drying by infrared lamp irradiation, the CuBr/ITO photocathode was obtained.

2.3. Preparation of the $Aptamer_{(AFB1)}$−PMSN−$[Fe(CN)_6]^{3-}$ Conjugate. First, mesoporous silicon dioxide nanospheres (MSNs) were synthesized via the following procedure.[37] A 0.1 g portion of CTAB was dissolved in 7 mL of ultrapure water. Subsequently, 1.8 mL of ethanol and 3 mL of ether were added. Then, 2 mL of TEOS and 0.1 mL of ammonia were dripped slowly. After vigorous stirring for 4 h, the mixture was centrifuged and washed with water and ethanol three times. The obtained MSNs were dried at 60 °C and annealed at 550 °C to remove the surfactant and form the inner channels. Afterward, the surface charge of MSNs was

https://doi.org/10.1021/acs.analchem.1c00503
Anal. Chem. 2021, 93, 6214−6222

Scheme 1. Schematic Diagram of the Multiplexed Self-Powered Biosensor with Dual-Photoelectrodes[a]

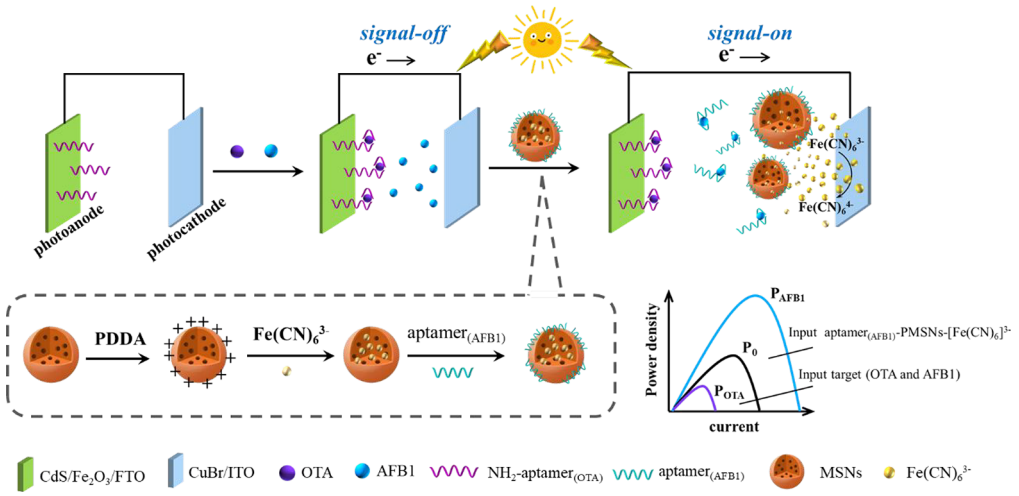

[a]The inset is the preparation process of the aptamer$_{(AFB1)}$−PMSN−$[Fe(CN)_6]^{3-}$ conjugate.

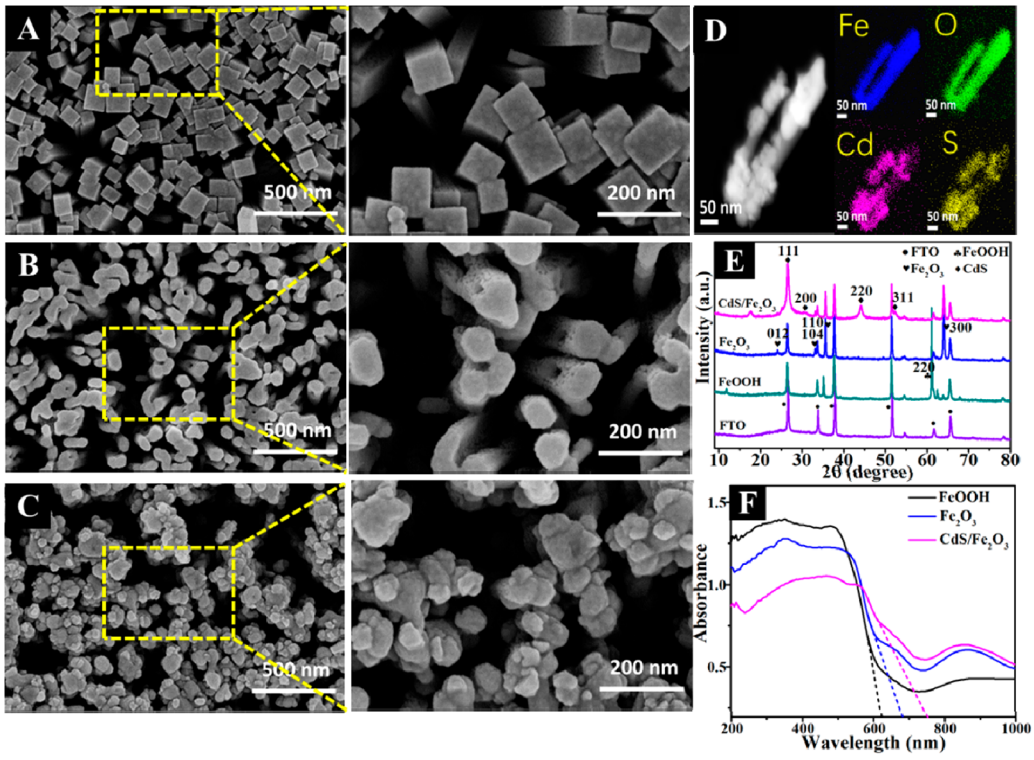

Figure 1. SEM image of FeOOH NRs/FTO (A), Fe_2O_3 NRs/FTO (B), and CdS/Fe_2O_3 NRs/FTO (C). (D) Elemental mapping of CdS/Fe_2O_3 NRs/FTO. (E) XRD of FTO, FeOOH NRs/FTO, Fe_2O_3 NRs/FTO, and CdS/Fe_2O_3 NRs/FTO. (F) UV−vis spectra of different photoanodes.

modified by PDDA. A 20 mg portion of MSNs was dispersed in 10 mL of 1% PDDA solution (0.02 mol/L NaCl), which was ultrasonicated for 30 min to obtain the positively charged MSNs (PMSNs). The product was then centrifuged, washed, and dried for future use.

Second, the aptamer$_{(AFB1)}$−PMSN−$[Fe(CN)_6]^{3-}$ conjugate was prepared. A 10 mg portion of PMSNs was dispersed in $[Fe(CN)_6]^{3-}$ solution (1 mL, 100 mmol/L) and shaken for 10 h at room temperature. In this process, $[Fe(CN)_6]^{3-}$ as the electron acceptor was diffused into the pores of PMSNs. Subsequently, 10 μL of 10 μmol/L aptamer$_{(AFB1)}$ was added and shaken for another 6 h. Therefore, the aptamer$_{(AFB1)}$ could be attached to the surface of PMSNs by electrostatic adsorption. The mixture was centrifuged and washed three times to remove residual aptamer$_{(AFB1)}$ and $[Fe(CN)_6]^{3-}$. Finally, the prepared aptamer$_{(AFB1)}$−PMSN−$[Fe(CN)_6]^{3-}$ conjugate was scattered in 1 mL of 0.01 mol/L PBS (pH 7.4) and stored at 4 °C for use.

2.4. Construction of a Multiplexed PFC-SPB and PFC Measurement. The construction of the multiplexed self-powered sensor was shown in Scheme 1. A 10 μL portion of 0.1% chitosan solution was coated on the CdS/Fe_2O_3 NRs/FTO photoanode. After drying by infrared lamp, 20 μL of 2.5% glutaraldehyde was dropped on the electrode as a cross-linking agent for the connection of NH_2−aptamer$_{(OTA)}$. After washing with 0.01 M PBS, the modified photoanode was incubated

https://doi.org/10.1021/acs.analchem.1c00503
Anal. Chem. 2021, 93, 6214−6222

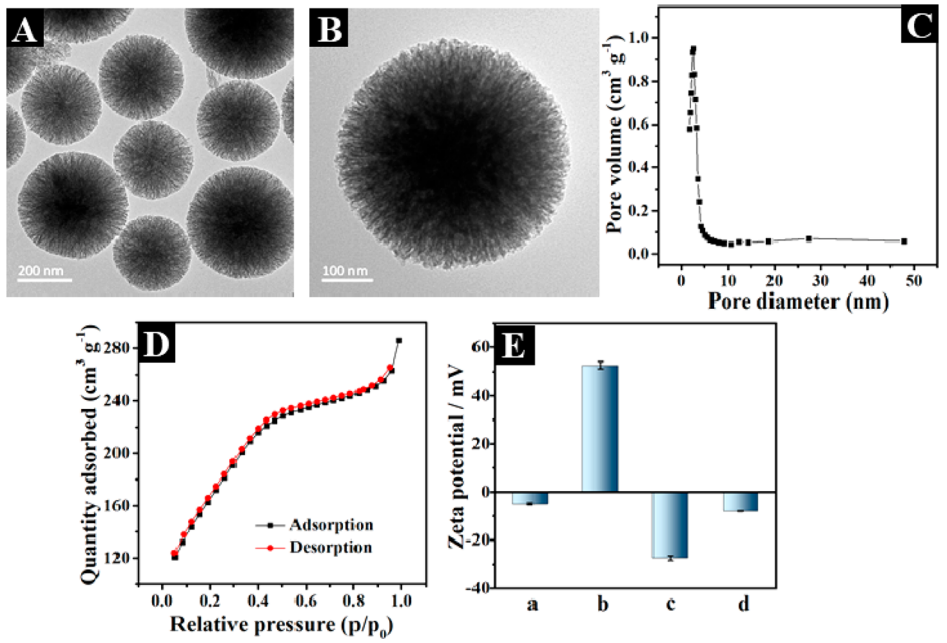

Figure 2. (A, B) TEM image of MSNs. (C) Pore size distribution of MSNs. (D) N_2 adsorption−desorption isotherm plot of MSNs. (E) Zeta potential of MSNs (a), PMSNs (b), aptamer$_{(AFB1)}$−PMSN−$[Fe(CN)_6]^{3-}$ conjugate (c), and aptamer$_{(AFB1)}$−PMSN−$[Fe(CN)_6]^{3-}$ conjugate incubated with AFB1 (d).

with 20 μL of 1 μmol/L NH_2-aptamer$_{(OTA)}$ for 12 h at 4 °C in a moisture atmosphere and then gently rinsed to remove the physically adsorbed aptamer. Subsequently, 20 μL of 3% BSA was used to block nonspecific binding sites. Finally, this aptamer$_{(OTA)}$ modified CdS/Fe_2O_3 NRs/FTO bio-photoanode and CuBr/ITO photocathode were introduced to an electrolytic cell with 0.1 mol/L PBS (pH 7.4) to form the single-chamber multiplexed self-powered sensor.

The PFC measurement was performed with a two-electrode system. Concretely, both the bio-photoanode and photocathode were irradiated vertically by a 500 W Xe lamp. The initial power density (P_0) was tested in 0.1 mol/L PBS (pH 7.4). For the detection of two mycotoxins, the photoanode was immersed in 200 μL of a mixture containing OTA and AFB1 with various concentrations and incubated at 37 °C for 30 min. The OTA concentration was determined by measuring the power density variation. Subsequently, 50 μL of aptamer$_{(AFB1)}$−PMSN−$[Fe(CN)_6]^{3-}$ conjugate was injected into the above solution and incubated at 37 °C for 1 h. Afterward, the mixture was added to 20 mL of supporting electrolyte, and the power density was measured again to determine the concentration of AFB1.

3. RESULTS AND DISCUSSION

3.1. Characterization of CdS/Fe_2O_3 NRs/FTO. The morphology of prepared CdS/Fe_2O_3 NRs/FTO was investigated by SEM under low and high magnifications. As can be perceived from Figure 1A, FeOOH NRs were grown vertically on the FTO surface with uniform size and high coverage. And these rod-shaped arrays presented a quadrilateral top with a side length of about 100 nm in local enlarged region. After calcination at high temperature (Figure 1B), these sharp four corners were passivated and became a circular top, indicating the transformation from FeOOH to Fe_2O_3 NRs. The microscopic growth morphologies of CdS modification were shown in Figure 1C; CdS nanoparticles were wrapped on each Fe_2O_3 NR, which significantly increased the diameter and roughness of rod structure. In addition, the image of TEM (Figure 1D) showed that CdS nanoparticles were deposited to the whole outer wall surface of one-dimensional nanorod from the top to the bottom. These increased specific surface areas could provide more active sites for the aptamer immobilization. The element mapping showed that CdS/Fe_2O_3 NRs were solid rods with a diameter of about 120 nm. The elements of Fe and O constituted the main body of the rod, while Cd and S were basically attached on the outer surface, forming a core−shell structure.

The phase and crystal structures of all samples were measured by powder X-ray diffraction (XRD) and shown in Figure 1E. Some characteristic peaks at 26.49, 33.74, 37.81, 51.56, 61.63, and 65.69° (JCPDS no. 77-0452), corresponding to SnO_2 from FTO substrate, could be observed in all samples. The formation of FeOOH was determined by the diffraction peak at 61.17°, indexing to the (220) peak of wustite (JCPDS no. 74-1880). After the annealing process, the peaks were found at 24.15, 33.16, 35.63, and 64.00°, assigning to the (012), (104), (110), and (300) planes of Fe_2O_3 with hematite structure (JCPDS no. 87-1165). For CdS/Fe_2O_3 NRs/FTO, some new diffraction peaks at about 26.55, 30.75, 44.04, and 52.16° were well matched with the (111), (200), (220), and (311) planes of CdS (JCPDS No. 80-0019), indicating the successful modification of CdS on Fe_2O_3 NRs.

Figure 1F showed the optical properties of the above samples measured by UV−vis spectrophotometry in the range 200−1000 nm, where FeOOH had an absorption edge around 620 nm. With the formation of Fe_2O_3 and the enhancement of crystallinity during the calcination process, the Fe_2O_3 presented a wider absorption edge of about 680 nm and a narrower E_g of 2.2 eV.[38] After modification by CdS nanoparticles, the spectrum of CdS/Fe_2O_3 NRs/FTO was further shifted toward the long-wavelength region, exhibiting absorption edges close to 750 nm as the estimated E_g of 2.4 eV.[39] The results show that the deposition of CdS on the

https://doi.org/10.1021/acs.analchem.1c00503
Anal. Chem. 2021, 93, 6214−6222

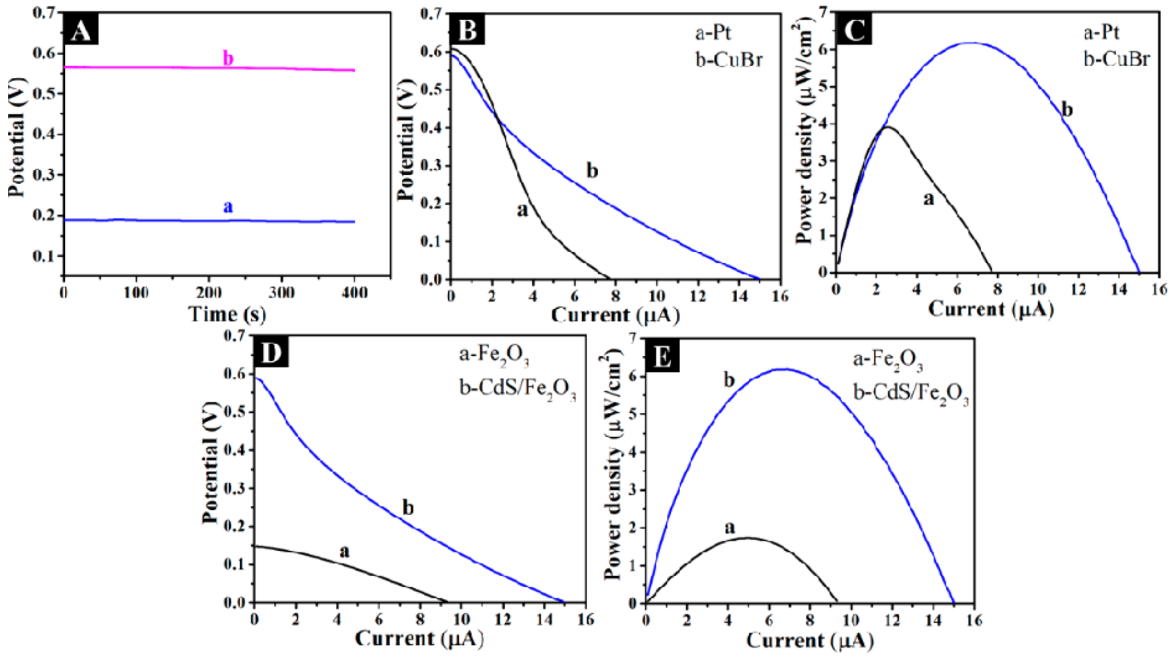

Figure 3. (A) OCP of the prepared PFC-SPB without (curve a) and with (curve b) photoirradiation. (B) *V*−*I* and (C) *P*−*I* curves of the PFC-SPB with the CdS/Fe_2O_3 NRs/FTO photoanode and different photocathodes: Pt (a) and CuBr/ITO (b). (D) *V*−*I* and (E) *P*−*I* curves of the PFC-SPB with the CuBr/ITO photocathode and different photoanodes: Fe_2O_3 NRs/FTO (a) and CdS/Fe_2O_3 NRs/FTO (b).

surface of Fe_2O_3 NRs could improve the photoabsorption, promote the electron−hole separation, and enhance the signal response.

3.2. Characterization of the Aptamer$_{(AFB1)}$−PMSN−$[Fe(CN)_6]^{3-}$ Conjugate. Based on the improvement of our previous work, MSNs were prepared via the sol−gel method.[37] As shown in Figure 2A, the MSNs presented a uniform morphology of mesoporous nanospheres with a mean size of about 250 nm. From the local magnification (Figure 2B), it could be seen that the product had a rough surface and fine pores. A large number of silica nanoflakes grew radially from the center to the periphery, forming mesoporous nanospheres with many folds on the surface. These folds provide more specific surface area for aptamer immobilization, while the ordered channels provide more space for the loading of electron acceptor ($[Fe(CN)_6]^{3-}$). The pore size distribution plot and N_2 adsorption−desorption isotherm were investigated in Figure 2C and D. The average pore size was about 2.9 nm with the Brunauer−Emmett−Teller (BET) surface area of 604 m^2/g, which was suitable for the encapsulation of $[Fe(CN)_6]^{3-}$.[40] In order to prove the successful preparation of the aptamer$_{(AFB1)}$−PMSN−$[Fe(CN)_6]^{3-}$ conjugate and the feasibility of target trapping, the zeta-potentials of each step were determined. As shown in Figure 2E, after PDDA modification, the zeta-potential of the MSNs was reversed from −4.9 to +52.6 mV due to the adsorption of the PDDA layer with positive charge. Another reversal occurred when $[Fe(CN)_6]^{3-}$ was encapsulated in PMSNs and sealed with aptamer$_{(AFB1)}$. This may be due to the negative charge of phosphate backbones in aptamers.[41] In the presence of the targets, the aptamers adsorbed by electrostatic adsorption fell off, so the electronegativity of the conjugate could recover to a certain extent. These phenomena proved the successful preparation of the aptamer$_{(AFB1)}$−PMSN−$[Fe(CN)_6]^{3-}$ conjugate and the ability of the aptamer to capture the target.

3.3. Mechanism of the Multiplexed PFC-SPB. A multiplexed self-powered sensor based on a dual-photoelectrode internal-driven photocatalytic fuel cell was constructed for simultaneous detection of OTA and AFB1. As in Scheme 1, this platform was assembled in a single-chamber cell with aptamer$_{(OTA)}$/CdS/Fe_2O_3 NRs/FTO as the bio-photoanode, CuBr/ITO as the photocathode, and aptamer$_{(AFB1)}$−PMSN−$[Fe(CN)_6]^{3-}$ conjugate as the signal probe. In the probe design, PMSNs were used as the carriers and $[Fe(CN)_6]^{3-}$ could be diffused into the channels of PMSNs. Due to the positive charges of PDDA, the aptamers with negative charge could be fixed on the surface of PMSNs by electrostatic adsorption and act as a biological gate to seal $[Fe(CN)_6]^{3-}$ in the channels. When two kinds of targets existed simultaneously, OTA would be captured and attached to the bio-photoanode surface by the specific recognition of aptamer$_{(OTA)}$. Based on the steric hindrance effect, the electronic transmission between the solid−liquid interfaces was affected, thus reducing the signal response and realizing the detection of OTA. Subsequently, the conjugate probe was added to the electrolyte. After aptamer$_{(AFB1)}$ combined with AFB1, the aptamers were detached from the surface of the PMSNs, and the electron acceptors encapsulated in the channels were released, which accelerated the electron transfer of the external circuit and improved the signal response, thus realizing the sensitive detection of AFB1.

In order to explore the performance of this PFC-SPB, the influence of light irradiation was investigated. As shown in Figure 3A, the open circuit potential (OCP) of the PFC-SPB with photoirradiation (curve b) was about 3 times of that without illumination (curve a). Therefore, the excitation of light had a significant effect on the generation of electricity in the system and was conducive to driving the migration of electrons on the two photoelectrodes, so as to improve the signal response. In addition, the output signal based on different photoanodes and photocathodes was also inves-

https://doi.org/10.1021/acs.analchem.1c00503
Anal. Chem. 2021, 93, 6214−6222

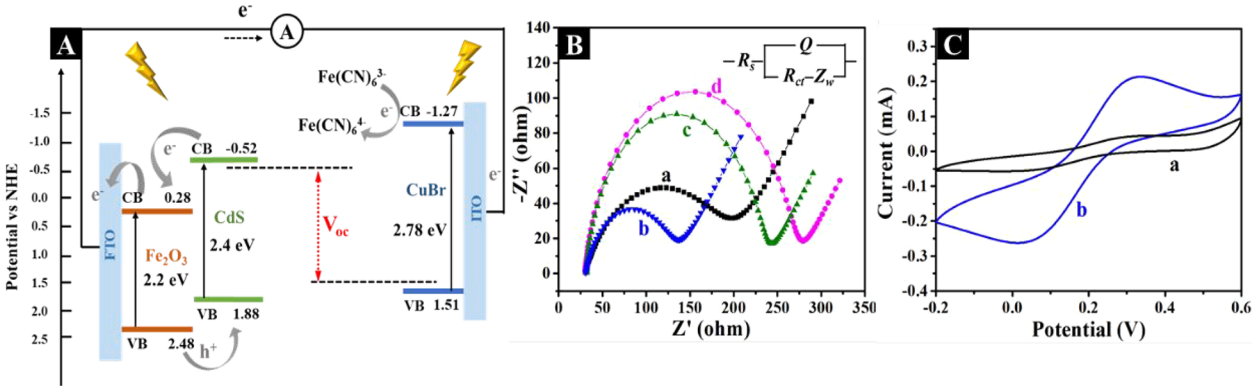

Figure 4. (A) Schematic diagram of the energy level and the response mechanism of the PFC-SPB. (B) EIS spectra of Fe_2O_3 NRs/FTO (a), CdS/Fe_2O_3 NRs/FTO (b), aptamer$_{(OTA)}$/CdS/Fe_2O_3 NRs/FTO (c), and OTA/aptamer$_{(OTA)}$/CdS/Fe_2O_3 NRs/FTO (d). (C) Cyclic voltammograms of $[Fe(CN)_6]^{3-}$ at the cathode in the absence (a) and presence (b) of AFB1.

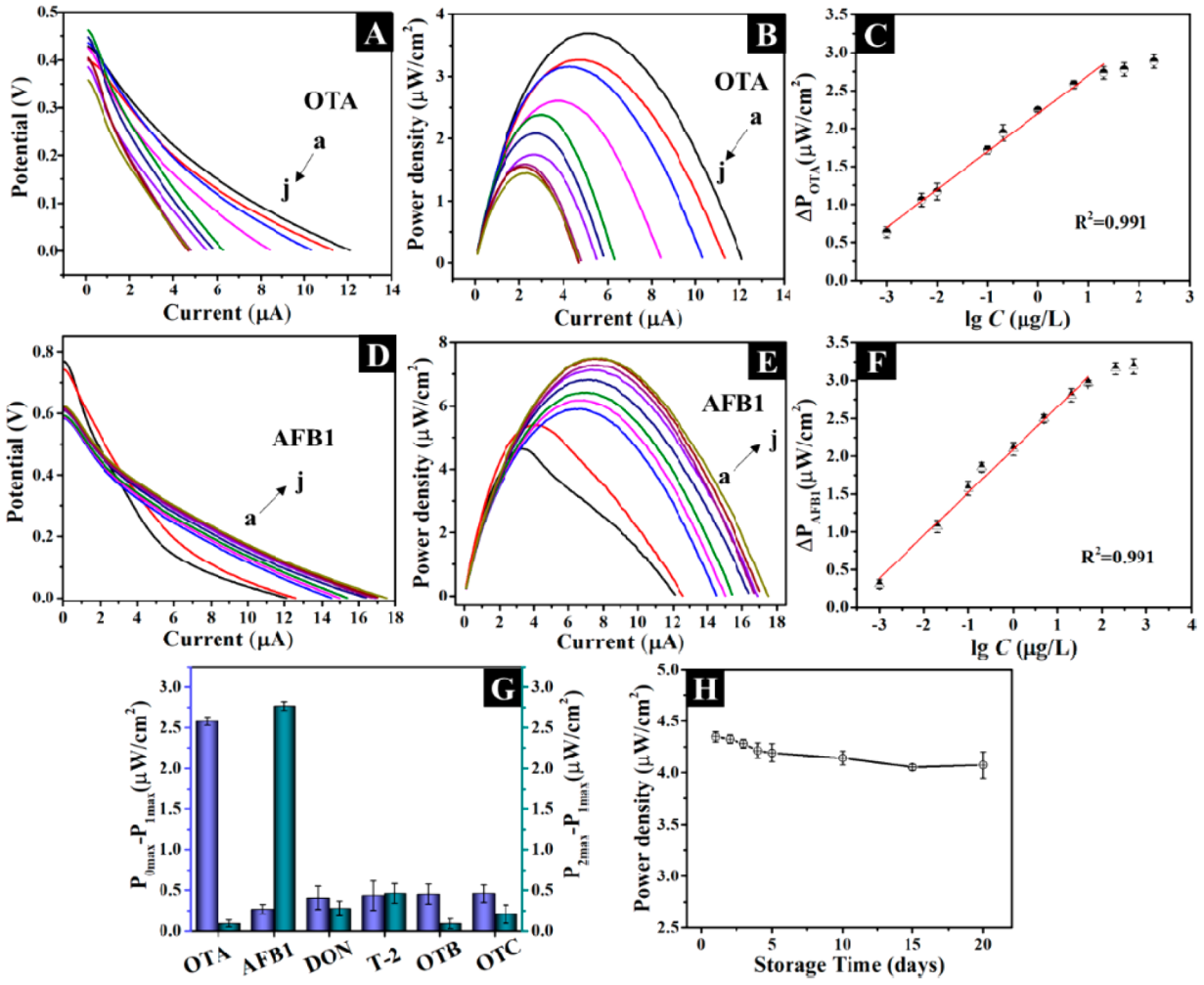

Figure 5. *V*–*I* (A) and *P*–*I* (B) responses for different concentrations of OTA: (a) 0.001, (b) 0.005, (c) 0.01, (d) 0.1, (e) 0.2, (f) 1, (g) 5, (h) 20, (i) 50, and (j) 200 μg/L in PBS (0.1 mol/L, pH 7.4) at a bias potential of 0 V. (C) Relationship between ΔP_{OTA} and the logarithm of OTA concentration. The *V*–*I* (D) and *P*–*I* (E) responses for different concentrations of AFB1: (a) 0.001, (b) 0.02, (c) 0.1, (d) 0.2, (e) 1, (f) 5, (g) 20, (h) 50, (i) 200, and (j) 500 μg/L in PBS (0.1 mol/L, pH 7.4) at a bias potential of 0 V. (F) Relationship between ΔP_{AFB1} and the logarithm of AFB1 concentration. The selectivity (G) and the stability (H) evaluation of the constructed multiplexed self-powered sensor.

tigated. As shown in Figure 3B and C, both of them used CdS/Fe_2O_3 NRs/FTO as the photoanode. Compared with the output voltage and power density of the traditional Pt electrode (curve a) and CuBr/ITO photocathode (curve b), it could be seen that the maximum output power density (P_{max}) of prepared dual-photoelectrodes PFC-SPB based on CuBr/ITO as the photocathode was significantly higher than that of the single photoelectrode PFC-SPB based on the Pt electrode. These results showed that the strategy of a dual-photoelectrode construction had stronger absorption and

https://doi.org/10.1021/acs.analchem.1c00503
Anal. Chem. 2021, 93, 6214−6222

conversion ability for visible light and could effectively improve the utilization of optical energy. The CuBr/ITO photocathode represented excellent performance by matching the photoanode with an appropriate energy level. Moreover, from Figure 3D and E, the responses under different photoanode constructions were shown. With CuBr/ITO as the photocathode and Fe_2O_3 NRs/FTO as the photoanode, P_{max} was 1.73 $\mu W/cm^{-2}$. However, the PFC-SPB constructed by CdS/Fe_2O_3 NRs/FTO exhibited about 3.6 times of P_{max}, with the value up to 6.18 $\mu W/cm^{-2}$. This may be due to the modification of CdS nanoparticles enhancing the light absorption effectively. Compared with the pure Fe_2O_3 NRs, the heterojunction of CdS and Fe_2O_3 could effectively suppress the recombination of electron−hole pairs and expedite the charge separation and migration.

The detailed mechanism of electronic transmission between interfaces was shown in Figure 4A. When the two photoelectrodes were irradiated, the electrons in the valence band (VB) of the photoanode and photocathode could be excited concurrently and jumped to their conduction band (CB), respectively, to form the electron−hole pairs. Due to the stronger electronegativity of CdS than that of Fe_2O_3, photogenerated electrons could be quickly transferred from the CB of CdS (−0.52 V vs NHE) to that of Fe_2O_3 (0.28 V vs NHE)[42] and then injected into the FTO. Based on the large Fermi level deviation between the photoanode and photocathode (the Fermi levels of the photoanode and photocathode are close to the CB of CdS and the VB of CuBr),[43] the electrons were transferred to the photocathode through the external circuit. Subsequently, these electrons accumulated on the CB of CuBr (−1.27 V vs NHE) could be consumed timely and effectively by the reduction of $[Fe(CN)_6]^{3-}$, thus promoting the generation and migration of electrons between the two photoelectrodes and enhancing the response.

In order to verify the feasibility of this PFC-SPB, the interfacial characteristics and signal variation of the photoanode and photocathode were investigated. As shown in Figure 4B, the stepwise assembly process of the bio-photoanode was demonstrated by the impedance spectrum. The electron-transfer resistance (R_{et}) value of CdS/Fe_2O_3 NRs/FTO was smaller than that of Fe_2O_3 NRs/FTO, indicating the modification of CdS is helpful for the separation and transfer of electrons, and the output signal of the heterojunction is significantly greater than that of the monomer Fe_2O_3. After the $aptamer_{(OTA)}$ was fixed on the photoanode surface, the R_{et} value increased to 245 Ω, due to the steric hindrance effect caused by aptamers. When the target was captured, the value of R_{et} continued to increase, suggesting that OTA attached to the photoanode surface could inhibit the transport between interfaces. These reasonable variations in R_{et} explained that the proposed self-powered sensor was feasible in OTA detection. In addition, cyclic voltammograms (CVs) were used to investigate the signal change of the photocathode. In Figure 4C, in the absence of AFB1, the electron acceptor was encapsulated in the PMSNs, so a pair of small redox peaks were obtained. After AFB_1 was added, the $aptamer_{(AFB1)}$ hybridized with the target and separated from the surface of PMSNs. Then, $[Fe(CN)_6]^{3-}$ as electron acceptor was released; thus, the peak current was significantly enhanced. These responses have indicated that this multiplexed PFC-SPB could realize the simultaneous detection of OTA and AFB1.

3.4. Analytical Performance of the Multiplexed PFC-SPB. Based on the dual-photoelectrode internal-driven photocatalytic fuel cell, the simultaneous detection of OTA and AFB_1 was realized under the optimal experimental conditions (the detailed analysis could be found in the Supporting Information, Figure S1). The $V-I$ and $P-I$ curves were investigated in Figure 5A and B. With the increase of OTA concentration, more OTA−aptamer complexes were attached on the photoanode, which increased the steric effect and suppressed the electron transport between the solid−liquid interfaces, thus resulting in the decrease of short-circuit current density and power density. In Figure 5C, the change of maximum output power density caused by OTA (ΔP_{OTA}) was proportional to the OTA concentration ($\Delta P_{OTA} = P_{0max} - P_{1max}$, where P_{0max} and P_{1max} represented the maximum output power density in the absence and presence of a target, respectively). When the concentration of OTA was between 1 ng/L and 20 μg/L, ΔP_{OTA} was linearly correlated with the logarithm of OTA concentration. The regression equation of OTA was calculated to be $\Delta P_{OTA} = 2.20 + 0.50[\log C_{OTA}\ (\mu g/L)]$ with a correlation coefficient of 0.991 and a detection limit of 0.18 ng/L (S/N = 3). Moreover, as shown in Figure 5D and E, with the increase of AFB1 concentration, more $[Fe(CN)_6]^{3-}$ was released into the electrolyte, which accelerated the electron transfer between the photoanode and photocathode, thus increasing the short-circuit current density and power density. In Figure 5F, ΔP_{AFB1} ($\Delta P_{AFB1} = P_{2max} - P_{1max}$, where P_{2max} represented the maximum output power density after incubation of $aptamer_{(AFB1)}$−PMSN−$[Fe(CN)_6]^{3-}$ conjugate) was positively proportional to AFB1 concentration, and a good linear relationship was obtained between ΔP_{AFB1} and the logarithm of AFB1 concentration in the range from 1 ng/L to 50 μg/L. The regression equation of AFB1 was calculated to be $\Delta P_{AFB1} = 2.09 + 0.57[\log C_{AFB1}\ (\mu g/L)]$ with a correlation coefficient of 0.991 and a detection limit of 0.82 ng/L (S/N = 3). Due to the efficient light utilization, simple operation, and multitarget recognition, this self-powered sensor could provide a more comprehensive and convenient detection method for mycotoxin pollution in agricultural products. Compared with the published reports (Table S1), this work exhibited a wider detection range and lower detection limit. Especially, it achieved a multitarget analysis, while most of the previous work could detect only one target (OTA or AFB1). Its multitarget recognition ability benefitted from the application of an electron-transfer-regulated conversion strategy in the design of the PFC-SPB, so that the response of each recognition element could be distinguished without mutual interference. In addition, the dual-photoelectrodes with excellent photoelectric conversion properties could enhance the absorption and utilization of light energy, so as to improve the sensor performance. And this membrane free single-chamber structure further promoted the development of PFC-SPBs to miniaturization and integration.

The selectivity of the prepared PFC was investigated by mycotoxins such as deoxynivalenol (DON), T-2 toxin (T-2), ochratoxin B (OTB), and ochratoxin C (OTC) at the same concentration of 5 μg/L, respectively. As shown in Figure 5G, the responses of these interferents were much lower than those of OTA and AFB1, revealing that the ΔP_{max} was caused by the specific recognition of aptamers. Therefore, this method had high specificity and anti-interference ability. In addition, the long-term stability of the self-powered sensor was shown in Figure 5H. After the photoelectrodes were kept at 4 °C for 3 weeks, the value of P_{max} could still maintain 94% of the initial

https://doi.org/10.1021/acs.analchem.1c00503
Anal. Chem. 2021, 93, 6214−6222

response, showing the excellent robustness and long-term storage stability.

To evaluate the practicability and reliability of this sensing platform, the recoveries of OTA and AFB1 in maize were assessed by the standard addition method. The corn kernels were purchased from a local market. After full crushing, the 25 g of corn flour was mixed with 5 g of NaCl evenly and then transferred into a volumetric flask and diluted to 100 mL with 80% methanol. Subsequently, the mixture was homogenized and extracted at high speed for 2 min. After filtration, the extract was diluted 5 times for future use. Prior to the addition of standard solution at each concentration, the liquid chromatography−mass spectrometry was used to ensure that there was no OTA and AFB1 contamination. Then, 0.5 μg/L of OTA, AFB1, and their mixture (containing 0.3 μg/L of OTA and 0.3 μg/L of AFB1) was added into the extract samples and tested directly without any pretreatments. As shown in Table S2, the recoveries were 95.2% with the RSD of 6.3% for OTA, 97.4% with the RSD of 6.2% for AFB1, and 105.3−109.5% with the RSD of 3.0−5.9% for the mixed sample. These results demonstrated that the self-powered sensor can be used for the simultaneous detection of two mycotoxins in real samples.

4. CONCLUSIONS

In summary, a multiplexed dual-photoelectrode PFC-SPB based on the electron-transfer-regulated conversion strategy for simultaneous detection of OTA and AFB1 was designed, which was composed of the CdS/Fe_2O_3 NRs/FTO photoanode and CuBr photocathode in a membrane free single chamber. This proposed PFC-SPB exhibited a wide linear range of 1 ng/L to 20 μg/L for OTA detection and 1 ng/L to 50 μg/L for AFB1 detection with the detection limit of 0.18 ng/L for OTA and 0.82 ng/L for AFB1. Its excellent selectivity, sensitivity, and multitarget recognition ability benefited from the following aspects: (1) Based on the electron-transfer-regulated conversion strategy, the signal response of each recognition element could be distinguished. And this strategy was not highly dependent on the type of photoactive materials, the precision of electrode modification, and the performance of light sources. (2) No external voltage was required for the application process, which prevented the nonspecific redox reaction of some electroactive interferents on the electrode surface, thus obtaining a higher selectivity. (3) The structure of a dual-photoelectrode system and membrane free single chamber could shrink the device dimension, which provided a new construction strategy for the development of miniaturized devices. (4) The photoanode and photocathode with a high efficiency of photoelectric conversion could improve the utilization of light energy, enhance the sensitivity of analysis, and avoid the expensive Pt electrode. In a word, this sensor was low-cost and time-saving, which not only exhibited the comprehensive and accurate results for mycotoxin contaminated samples but also provided a useful perspective for the development of a multiplexed self-powered sensor.

ASSOCIATED CONTENT

Supporting Information

The Supporting Information is available free of charge at https://pubs.acs.org/doi/10.1021/acs.analchem.1c00503.

Detailed descriptions regarding the materials and instruments, optimization of detection conditions, comparison of available biosensors for analysis of OTA and AFB1, and recoveries of OTA and AFB1 in maize samples from the as-prepared multiplexed self-powered biosensor (PDF)

AUTHOR INFORMATION

Corresponding Author

Kun Wang − *Key Laboratory of Modern Agriculture Equipment and Technology, School of Chemistry and Chemical Engineering, Jiangsu University, Zhenjiang 212013, PR China;* orcid.org/0000-0001-6764-8686; Email: wangkun@ujs.edu.cn

Authors

Jie Wei − *Key Laboratory of Modern Agriculture Equipment and Technology, School of Chemistry and Chemical Engineering, Jiangsu University, Zhenjiang 212013, PR China*

Qinqin Hu − *Key Laboratory of Modern Agriculture Equipment and Technology, School of Chemistry and Chemical Engineering, Jiangsu University, Zhenjiang 212013, PR China*

Yun Gao − *Key Laboratory of Modern Agriculture Equipment and Technology, School of Chemistry and Chemical Engineering, Jiangsu University, Zhenjiang 212013, PR China*

Nan Hao − *Key Laboratory of Modern Agriculture Equipment and Technology, School of Chemistry and Chemical Engineering, Jiangsu University, Zhenjiang 212013, PR China*

Jing Qian − *Key Laboratory of Modern Agriculture Equipment and Technology, School of Chemistry and Chemical Engineering, Jiangsu University, Zhenjiang 212013, PR China;* orcid.org/0000-0002-4472-6044

Complete contact information is available at: https://pubs.acs.org/10.1021/acs.analchem.1c00503

Notes

The authors declare no competing financial interest.

ACKNOWLEDGMENTS

We gratefully acknowledge the National Natural Science Foundation of China (Nos. 21375050 and 21675066), Project Funded by the Priority Academic Program Development of Jiangsu Higher Education Institutions (No. PAPD-2018-87), the Special Foundation of China Postdoctoral (No. 2019TQ0127), and the China Postdoctoral Science Foundation (No. 2020M671368).

REFERENCES

(1) Yan, K.; Ji, W.; Zhu, Y.; Chen, F.; Zhang, J. *Chem. Commun.* **2019**, *55* (80), 12040−12043.

(2) Zhang, J.; Wang, Z.; Chu, L.; Chen, R.; Zhang, C.; Toan, S.; Bagley, D.; Sun, J.; Dong, S.; Fan, M. *J. Power Sources* **2021**, *481*, 229133.

(3) Hao, N.; Dai, Z.; Meng, X.; Hua, R.; Lu, J.; Wang, K. *Sens. Actuators, B* **2020**, *306*, 127594.

(4) Soares, R. R. A.; Hjort, R. G.; Pola, C. C.; Parate, K.; Reis, E. L.; Soares, N. F. F.; McLamore, E. S.; Claussen, J. C.; Gomes, C. L. *ACS Sens.* **2020**, *5* (7), 1900−1911.

(5) Wei, J.; Liu, S.; Qileng, A.; Qin, W.; Liu, W.; Wang, K.; Liu, Y. *Sens. Actuators, B* **2021**, *330*, 129380.
(6) Yan, K.; Zhu, Y.; Ji, W.; Chen, F.; Zhang, J. *Anal. Chem.* **2018**, *90* (16), 9662−9666.
(7) Chen, Y.; Ji, W.; Gao, J.; Yan, K.; Zhang, J. *Chem. Commun.* **2020**, *56* (69), 10034−10037.
(8) Efrati, A.; Lu, C.-H.; Michaeli, D.; Nechushtai, R.; Alsaoub, S.; Schuhmann, W.; Willner, I. *Nat. Energy* **2016**, *1* (2), 15021.
(9) Xie, S.; Ouyang, K.; Ye, X. *J. Colloid Interface Sci.* **2018**, *532*, 758−766.
(10) Yan, K.; Yang, Y.; Okoth, O. K.; Cheng, L.; Zhang, J. *Anal. Chem.* **2016**, *88* (12), 6140−6144.
(11) Dai, W. X.; Zhang, L.; Zhao, W. W.; Yu, X. D.; Xu, J. J.; Chen, H. Y. *Anal. Chem.* **2017**, *89* (15), 8070−8078.
(12) Ji, W.; Yan, K.; Chen, Y.; Gao, J.; Zhang, J. *Sens. Actuators, B* **2019**, *292*, 129−135.
(13) Wang, Y.; Zhang, L.; Cui, K.; Xu, C.; Li, H.; Liu, H.; Yu, J. *Nanoscale* **2018**, *10* (7), 3421−3428.
(14) Gai, P.; Zhang, S.; Yu, W.; Li, H.; Li, F. *J. Mater. Chem. B* **2018**, *6* (42), 6842−6847.
(15) Du, X.; Jiang, D.; Liu, Q.; Hao, N.; Wang, K. *Anal. Chem.* **2019**, *91* (3), 1728−1732.
(16) Zhang, M.; Zhang, Z.; Xu, Y.; Wen, Z.; Ding, C.; Guo, Y.; Wang, K. *Biosens. Bioelectron.* **2020**, *156*, 112135.
(17) Du, X.; Zhang, B.; Jiang, D.; Sun, J. *Biosens. Bioelectron.* **2020**, *165*, 112414.
(18) dos Santos, G. K. C.; da Silva, F. G. S.; Yotsumoto Neto, S.; dos Santos, W. T. P.; de Cassia Silva Luz, R.; Damos, F. S. *Electroanalysis* **2018**, *30* (8), 1750−1756.
(19) Wang, P.; Han, P.; Dong, L.; Miao, X. *Electrochem. Commun.* **2015**, *61*, 36−39.
(20) Chang, J.; Wang, X.; Wang, J.; Li, H.; Li, F. *Anal. Chem.* **2019**, *91*, 3604−3610.
(21) Li, X.; Lu, J.; Feng, L.; Zhang, L.; Gong, J. *Anal. Chem.* **2020**, *92* (16), 11476−11483.
(22) Qian, J.; Cui, H.; Lu, X.; Wang, C.; An, K.; Hao, N.; Wang, K. *Chem. Eng. J.* **2020**, *401*, 126017.
(23) Liang, W.; Fan, C.; Zhuo, Y.; Zheng, Y.; Xiong, C.; Chai, Y.; Yuan, R. *Anal. Chem.* **2016**, *88*, 4940−4948.
(24) Zheng, Y.; Liang, W.; Yuan, Y.; Xiong, C.; Xie, S.; Wang, H.; Chai, Y.; Yuan, R. *Biosens. Bioelectron.* **2016**, *81*, 423−430.
(25) Hua, R.; Hao, N.; Lu, J.; Qian, J.; Liu, Q.; Li, H.; Wang, K. *Biosens. Bioelectron.* **2018**, *106*, 57−63.
(26) Wang, J.; Liu, Z.; Hu, C.; Hu, S. *Anal. Chem.* **2015**, *87*, 9368−9375.
(27) Lv, Y.; Zhou, Z.; Shen, Y.; Zhou, Q.; Ji, J.; Liu, S.; Zhang, Y. *ACS Sens.* **2018**, *3* (7), 1362−1367.
(28) Deng, H.; Huang, L.; Chai, Y.; Yuan, R.; Yuan, Y. *Anal. Chem.* **2019**, *91* (4), 2861−2868.
(29) Cao, J.; Ma, Y.; Lv, J.; Ren, S.; Liu, Y. *Chem. Commun.* **2020**, *56* (10), 1513−1516.
(30) Hao, N.; Hua, R.; Zhang, K.; Lu, J.; Wang, K. *Anal. Chem.* **2018**, *90* (22), 13207−13211.
(31) Gu, Y.; Ju, C.; Li, Y.; Shang, Z.; Wu, Y.; Jia, Y.; Niu, Y. *Biosens. Bioelectron.* **2015**, *66*, 24−31.
(32) Škrbić, B.; Živančev, J.; Đurišić-Mladenović, N.; Godula, M. *Food Control* **2012**, *25* (1), 389−396.
(33) Speijers, G. J.; Speijers, M. H. *Toxicol. Lett.* **2004**, *153* (1), 91−98.
(34) Sengling Cebin Coppa, C.; Mousavi Khaneghah, A.; Alvito, P.; Assunção, R.; Martins, C.; Eş, I.; Gonçalves, B.; Valganon de Neeff, D.; Sant'Ana, A.; Corassin, C.; Oliveira, C. *Trends Food Sci. Technol.* **2019**, *92*, 81−93.
(35) Qi, D.; Fei, T.; Liu, H.; Yao, H.; Wu, D.; Liu, B. *J. Agric. Food Chem.* **2017**, *65* (45), 9923−9929.
(36) Li, Z.; Su, C.; Wu, D.; Zhang, Z. *Anal. Chem.* **2018**, *90* (1), 961−967.
(37) Wei, J.; Chang, W.; Qileng, A.; Liu, W.; Zhang, Y.; Rong, S.; Lei, H.; Liu, Y. *Anal. Chem.* **2018**, *90* (15), 9606−9613.
(38) Bazrafshan, H.; Alipour Tesieh, Z.; Dabirnia, S.; Shajareh Touba, R.; Manghabati, H.; Nasernejad, B. *Powder Technol.* **2017**, *308*, 266−272.
(39) Kuang, P.; Zhang, L.; Cheng, B.; Yu, J. *Appl. Catal., B* **2017**, *218*, 570−580.
(40) Gai, P.; Gu, C.; Hou, T.; Li, F. *ACS Appl. Mater. Interfaces* **2018**, *10* (11), 9325−9331.
(41) Zhang, T.; Chai, H.; Meng, F.; Guo, Z.; Jiang, Y.; Miao, P. *ACS Appl. Mater. Interfaces* **2018**, *10* (43), 36796−36804.
(42) Xu, Y.; Schoonen, M. *Am. Mineral.* **2000**, *85* (3−4), 543−556.
(43) Li, F.; Li, Y. *J. Mater. Chem. C* **2015**, *3* (14), 3416−3421.

https://doi.org/10.1021/acs.analchem.1c00503
Anal. Chem. 2021, 93, 6214−6222